

University of Warsaw
Faculty of Physics

Kamila Kasperska
Record book number: 427907

Study of high-energy photons polarization in Compton scattering using the J-PET detector system

Bachelor's thesis in the field of Physics

The thesis was written under the supervision of
dr hab. Marcin Andrzej Konecki, prof. UW
Faculty of Physics
University of Warsaw
dr Magdalena Skurzok
Faculty of Physics, Astronomy and Applied Computer Science
Jagiellonian University in Kraków

Warsaw, June 2023

Summary

The purpose of this work is the study of the high-energy photons polarization in Compton scattering using the Jagiellonian Positron Emission Tomography scanner (J-PET), more specifically finding the distribution of an angle between incoming and scattered photons polarization planes which opens the door for the polarization studies. Although polarization itself is a well studied phenomenon, until now it was only possible to investigate it in a narrow range of energies, using optical methods. J-PET detector, due to its unique construction, allows the registration of high-energetic gamma quanta emitted by the radioactive source and coming from the electron-positron annihilation and also their multiple scatterings. It enables to determine the direction of photons momentum vectors, thus the directions of their polarization. In this work three main types of analysis were performed, differing in the energy and origin of the incoming photons: (i) electron-positron annihilation photons, with the energy of 511 keV, (ii) already scattered photons, found between two interactions in the detector with an unknown energy, (iii) ^{22}Ne de-excitation photons, with the energy of 1275 keV. Future measurements of the polarization will allow deeper understanding of the other phenomena, such as quantum entanglement or testing discrete symmetries in the leptonic sector.

Keywords

Photons, Polarization, Compton scattering, Positron emission tomography

Title of the thesis in Polish language

Badanie polaryzacji wysokoenergetycznych fotonów w rozpraszaniu Comptona za pomocą układu detekcyjnego J-PET

Contents

Introduction	3
1. Experimental setup	6
1.1. J-PET detector system	6
1.2. Experimental data	8
2. Methodology	10
2.1. Measurement of the linear polarization	10
2.2. Types of analysis	11
2.2.1. Analysis 1	11
2.2.2. Analysis 2	15
2.2.3. Analysis 3	16
2.3. Angle between polarization planes	17
3. Sequence selection accuracy	19
3.1. Monte Carlo simulation	19
3.2. Determination of sequence selection accuracy	19
4. Results	22
4.1. Analysis 1	22
4.2. Analysis 2	23
4.3. Analysis 3	23
5. Conclusions	25
6. Summary	26

Introduction

Polarization is one of the most interesting properties of photons, that allows us to show and understand several foundations of quantum mechanics [1, 2]. However, till now, mainly low-energy optical photons were studied in this respect. Thanks to the unique construction of the Jagiellonian Positron Emission Tomography scanner, the high-energy photons polarization can be investigated.

The aim of this work was to find the distribution of an angle between the polarization planes of incoming photon and its Compton scattering. For this purpose, measurements of linear polarization of photons were carried out.

Polarization is the relation between photon momentum vector and electric field vector. The linear polarization is characterized by the oscillations of the electric field in one plane, a plane containing the electric field vector and photon momentum [3]. This plane is called the polarization plane. The scheme of linear polarization with polarization plane marked is shown in Figure 1.

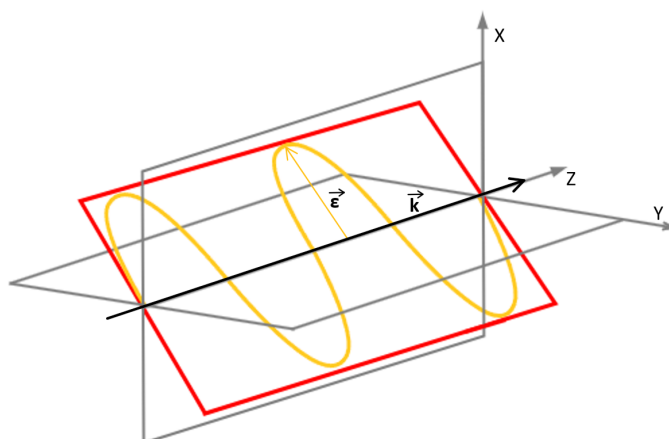


Figure 1: Scheme of linear polarization, where \vec{k} - photon momentum vector and $\vec{\epsilon}$ - polarization vector, electric field oscillations are marked yellow and polarization plane is marked red. Figure adapted from [3].

Due to the use of plastic scintillators, the photons interact with the detector predominantly via Compton scattering. In Compton scattering, a photon is scattered on a free or weakly bound electron, transferring a part of its energy to the electron. The energy of the scattered

gamma quantum is described by the formula:

$$E' = \frac{E}{1 + \frac{E}{m_e c^2} (1 - \cos \theta)}, \quad (1)$$

where E is the energy of the incoming gamma, $m_e = 511 \text{ keV}/c^2$ - electron's mass, θ - Compton scattering angle (angle between incoming and scattered photons momentum vectors).

Compton scattering enables to determine the direction of linear polarization of the incident photon (Section 2.1).

The differential cross section, thus the probability of the Compton scattering is described by the Klein-Nishina formula:

$$\frac{d\sigma_{KN}}{d\Omega} = \frac{r_0^2}{2} \left(\frac{E'}{E} \right)^2 \left(\frac{E}{E'} + \frac{E'}{E} - 2 \sin^2 \theta \cos^2 \eta \right), \quad (2)$$

where r_0 - classical electron radius, η - angle between the polarization vector ($\vec{\epsilon}$) of an incoming photon and scattering plane (a plane defined by incoming and scattered gamma quanta momentum vectors), E, E', θ - described as in Formula 1 [4]. The scheme of Compton scattering with scattering and polarization planes is shown in Figure 2.

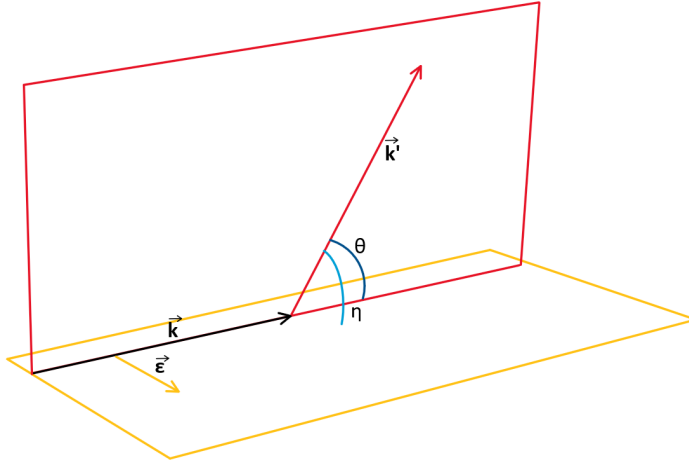


Figure 2: Scheme of Compton scattering, where \vec{k} - incident photon momentum vector, \vec{k}' - scattered photon momentum vector, θ - Compton scattering angle, $\vec{\epsilon}$ - incident photon's polarization vector. Initial and scattered photons momentum vectors form the scattering plane marked red. Incident photon momentum and polarization vector form the polarization plane marked yellow. The angle between the planes is denoted as η . Figure adapted from [5].

Further studies of high-energy photons polarization will enable the investigation of other phenomena, one of which is quantum entanglement of annihilation gamma quanta. Even though quantum entanglement was verified for many systems such as optical photons, the investigation of high-energy photons entanglement was thus far not possible. Measurements of linear polarization performed with the J-PET detector will allow deeper understanding of this phenomenon [6].

This thesis is organized as follows: chapter 1 contains the description of the J-PET detector and experimental data, chapter 2 describes the method of the analysis, chapter 3 contains the description of conducted simulation and estimated analysis accuracy, chapter 4 contains results of the analysis and chapter 5 concludes them.

Chapter 1

Experimental setup

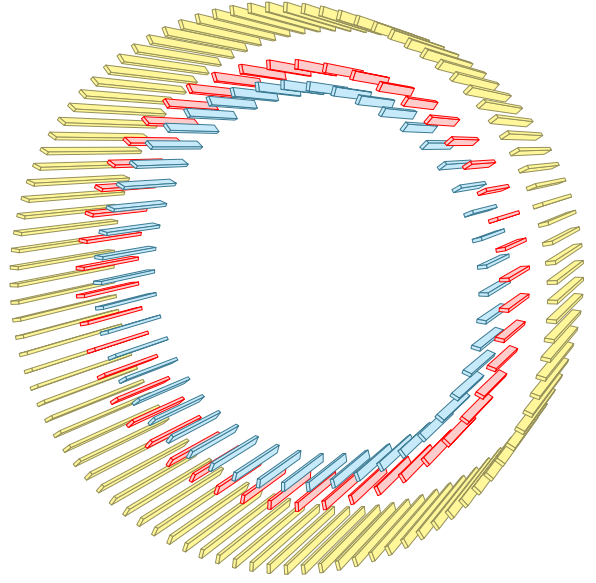
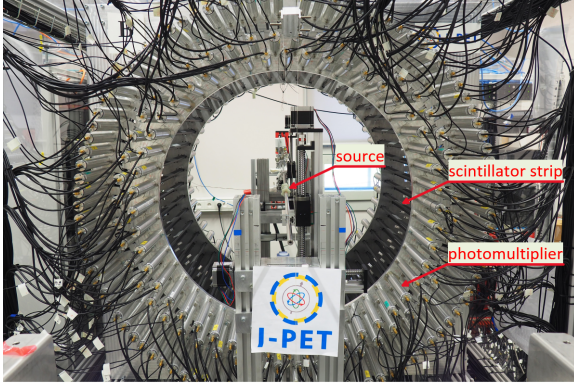
1.1. J-PET detector system

The Jagiellonian Positron Emission Tomography scanner (J-PET) is being developed in order to reduce the cost of the PET devices and enable universal access to diagnostics using positron emission tomography [7, 8].

Currently, all of the PET devices available on the market for radiation detection use crystal scintillators [9], the production cost of which is high. Therefore, the cost of the detector is high, and thus the access to diagnostics using the device is limited.

In addition to medical applications [10–12], the J-PET detector is also used for fundamental physics studies. J-PET detector allows to test discrete symmetries in the decays of positronium - an exotic atom consisting of electron and its anti-particle - positron [13]. Discrete symmetries can be tested by investigating discrete-symmetries-odd operators, constructed from ortho-positronium spin (Section 1.2) and the momentum and polarization vectors of annihilation photons [14].

The J-PET detector is a prototype of a tomograph built out of universally accessible and inexpensive organic scintillators. The use of this type of scintillators makes it possible to significantly reduce the production cost of the device. The device is built out of 192 scintillators with the dimensions of 0,7 cm - width, 1,9 cm - thickness and 50 cm - length. The scintillators are axially arranged, forming three coaxial cylinders that do not overlap. Diameters from the most internal layer are following: 85 cm, 93,5 cm and 115 cm. At both ends of the scintillator strip, photomultipliers are connected [15–17]. A photo and schematic view of the detector system is shown in Figure 1.1.



(a) Photo of the J-PET detector with source, scintillator strip and photomultiplier marked.

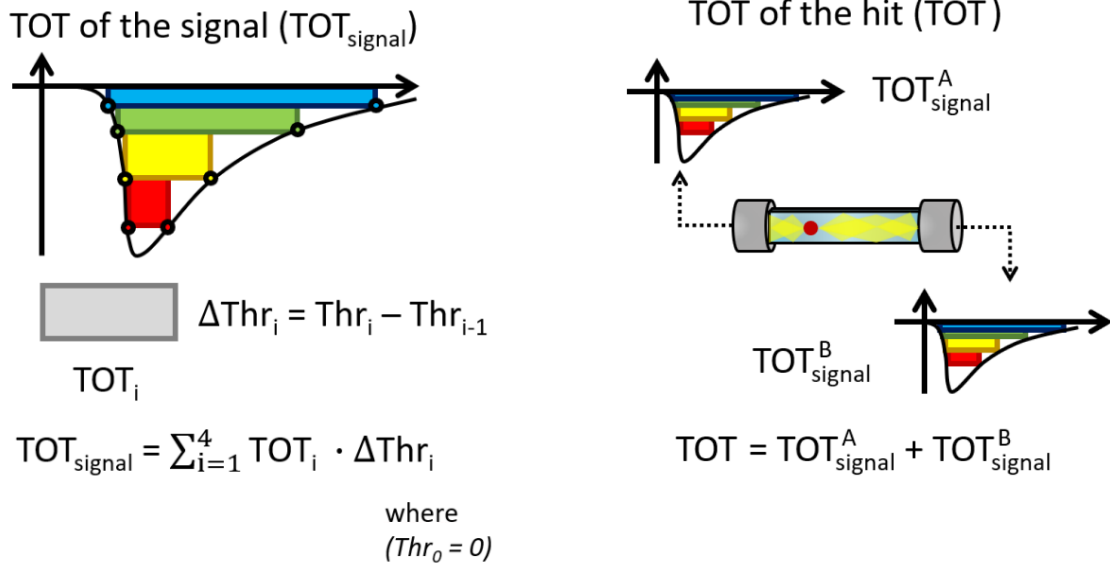
(b) J-PET detector scintillator strips layout. The detector consists of three cylindrical layers, layers 1 and 2 consist of 48 strips and layer 3 of 92 strips.

Figure 1.1: J-PET detector system.

As a result of Compton scattering, a photon transfers a part of its energy to an electron. The electron collides with atoms in matter, losing energy. The collisions result in excitation of atoms that de-excite into lower energy states by emitting photons. Light signals are emitted as a result of the interaction of a photon with a scintillator. The position of photon interaction along the scintillator strip is determined based on the time difference of those signals arriving at both photomultipliers [17]. The energy deposition is measured using the Time Over Threshold (TOT) method, in which the time difference between the leading and trailing edge of signal crossing given thresholds is measured (Figure 1.2). The TOT of the signal is calculated using the rectangular method, approximating to the area of the rectangle constructed at each threshold (Figure 1.2a) with an area $A = TOT_i \cdot \Delta Thr_i$, where $\Delta Thr_i = Thr_i - Thr_{i-1}$ assuming that $Thr_0 = 0$. The first height (ΔThr_i) is normalized to unity $\Delta Thr_1 = 1$ and the rest of the heights are normalized to the first threshold. As a measure of the energy deposition of gamma quanta, the total TOT value is used [18, 19]:

$$TOT = \sum_{PMT=A,B} \left(TOT_{PMT,1} + \sum_{i=2}^4 TOT_{PMT,i} \cdot \frac{\Delta Thr_i}{Thr_1} \right), \quad (1.1)$$

where $TOT_{PMT,i}$ represents the TOT value over all four thresholds measured by both photomultipliers (A, B) and Thr_i - threshold (Section 1.2).



(a) Illustration of the method of calculating TOT of the signal. (b) Illustration of the method of calculating total TOT of the hit.

Figure 1.2: Illustration of the analog signals obtained from the photomultipliers (PMTs) connected at both ends of the scintillator strip. Each signal's leading and trailing edge is probed at four thresholds. The TOT of the signal is calculated using the rectangular method (Equation 1.1). Figures and caption are adapted from [18, 19].

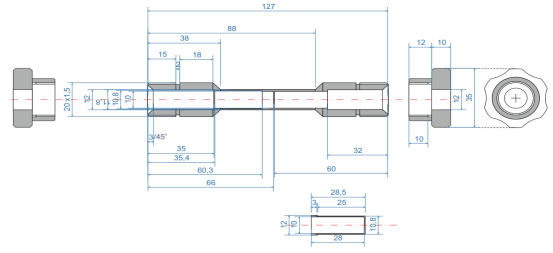
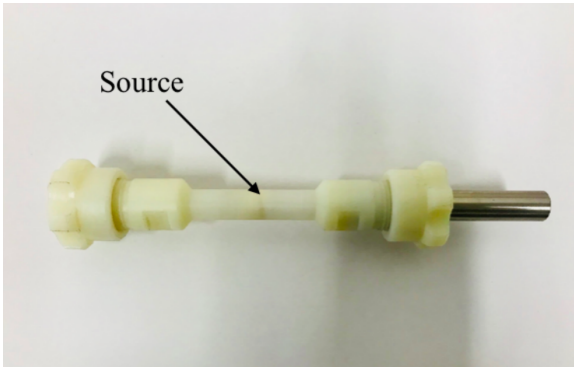
1.2. Experimental data

The experimental data that the analysis was performed on was from the Run 11 measurement. The Run 11 last from 02.04.2020 to 01.03.2021 and the data was effectively collected for about 250 days. Thresholds set for this run were 30 mV, 80 mV, 190 mV and 300 mV. In this study, 5000 out of about 600000 files (0,83%) were analyzed [20].

In Run 11, the measurements were performed using the small annihilation chamber made of plastic PA6 polyamide, shown in Figure 1.3. The ^{22}Na with the activity of 0.702 MBq, was sandwiched between a layer of 3 mm thickness of XAD-4 porous polymer from both sides at the center of the chamber. The chamber was placed at the center of the detector as shown in Figure 1.1a [21].

The ^{22}Na source decay scheme is shown in Figure 1.4. Since the Sodium 22 decays predominantly via β^+ decay, it emits positrons. In the thermalization process, a positron entering the material slows down quickly to an energy of the order of meV. Thermalized positron annihilates directly with electrons from the environment, emitting two photons back to back, both with the energy of 511 keV [22]. Moreover, the source decays mostly to the excited state of the ^{22}Ne . Neon achieving ground state emits de-excitation photon, called prompt, with the energy of 1275 keV.

The direct electron-positron annihilation is not the only process that can occur. Thermalized positron can also create a positronium (Ps) with an electron from the environment.



(a) Photo of the small annihilation chamber. Picture adapted from [21].

(b) Schematic view of the small annihilation chamber. Picture adapted from [21].

Figure 1.3: Small annihilation chamber.

Positronium can exist in two spin states: a singlet state known as para-positronium (p-Ps) with the spin value equal to 0 and triplet state known as ortho-positronium (o-Ps) with the spin value equal to 1. Both states are unstable with the mean lifetime in vacuum values of 125 ps and 142 ns, respectively. Positronium atoms decay into 2 (p-Ps) or 3 (o-Ps) gamma quanta [23].

This work focuses on three cases that are described in the next Chapter (2.2): (i) photons originating from the annihilation into 2 gamma quanta, (ii) photons found between two interactions in the detector, (iii) ^{22}Ne de-excitation photons.

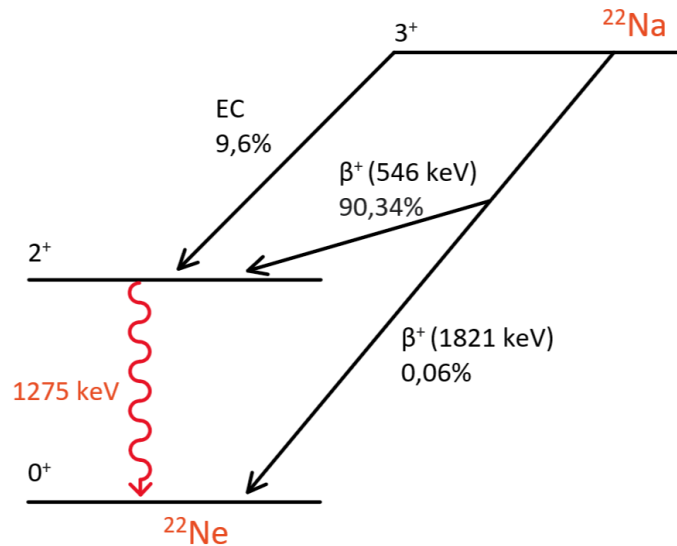


Figure 1.4: ^{22}Na decay scheme. Figure adapted from [18]

Chapter 2

Methodology

2.1. Measurement of the linear polarization

Since the Klein-Nishina formula (Equation 2) shows that the probability of Compton scattering is maximal for angles $\eta = 90^\circ$, it is assumed that it is always the case and that the incident photon polarization vector $\vec{\varepsilon}$ is perpendicular to the scattering plane and its direction is described as:

$$\vec{\varepsilon} = \frac{\vec{k} \times \vec{k}'}{|\vec{k} \times \vec{k}'|},$$

where \vec{k}, \vec{k}' - momentum vectors of incoming and scattered photons.

In order to find the angle between scattering planes of incoming and scattered gamma quanta, a sequence of three photons being each others successive scatterings is needed (Figure 2.1). The direction of the primary photon polarization vector is calculated as a cross product of primary and scattered photons momentum vectors: $\vec{\varepsilon} = \frac{\vec{k} \times \vec{k}'}{|\vec{k} \times \vec{k}'|}$ [5]. The scattering of the primary photon undergoes another Compton scattering and determination of its polarization vector is allowed. To determine the direction of the polarization vector of the first scattering ($\vec{\varepsilon}'$), the same method is used, with the use of the first and the second scattering of the primary photon: $\vec{\varepsilon}' = \frac{\vec{k}' \times \vec{k}''}{|\vec{k}' \times \vec{k}''|}$.

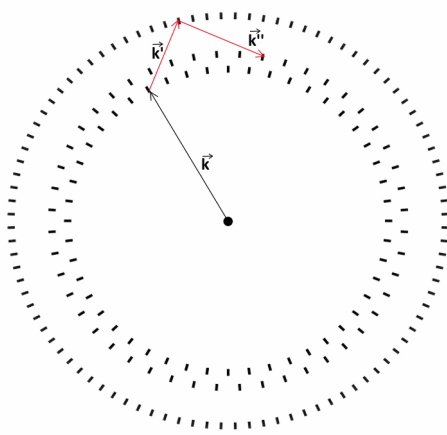


Figure 2.1: Schematic view of the J-PET detector's cross section with a scattering sequence starting with a photon originating from the source. Primary photon is marked black and its scatterings are marked red.

In frame of this work three types of analysis were performed, differing in the origin and energy of the primary (first in the sequence) photon. A sample of experimental and simulated data was analyzed.

2.2. Types of analysis

2.2.1. Analysis 1

For the Analysis 1, annihilation photon with the energy of 511 keV was chosen as a primary one.

The two annihilation photons emitted back-to-back can be detected as hits by two scintillator strips. To find the potential point of annihilation a line of response (line connecting two hits, LOR) was determined for every two hits in the analyzed data sample. The potential annihilation point was determined based on the time difference between two hits and lied at a distance:

$$d = \frac{1}{2}c(t_i - t_j)$$

from the center of LOR, where $c = 3 \cdot 10^8$ m/s - speed of light, t_i, t_j - times of hits registered by i, j -th strips (Figure 2.2).

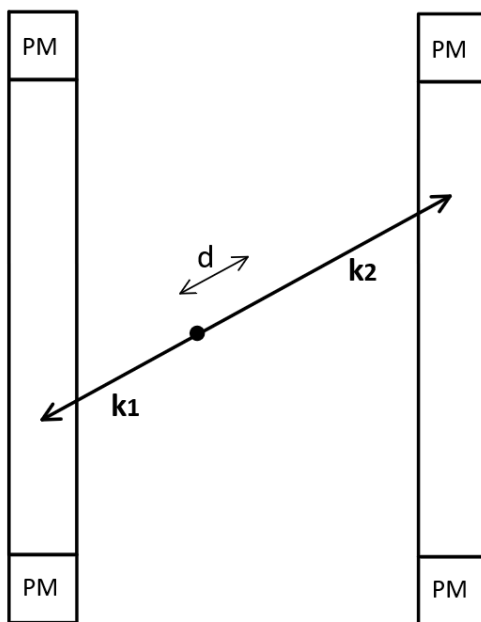


Figure 2.2: Schematic view of annihilation gamma quanta flight between two scintillators. As a black dot, annihilation point is marked, d - distance from the center of LOR, PM - photomultipliers. Figure adapted from [15].

Moreover, in order to select hits originating from the annihilation photons, a series of cuts was performed.

First, the cut on TOT value was applied. Maximal energy deposition (Compton edge) for the photons with the energy of 511 keV is $E_{depmax} = 340,67$ keV ($E_{dep} = E - E'$, see Formula 1). However, due to detector effects (its resolution), the Compton edge does not stop at 340,67 keV, which can be seen in Figure 2.3b. Therefore, energy deposition range for annihilation photon was chosen as 250 keV - 350 keV. Based on the formula describing the relation between TOT and energy deposition:

$$TOT(E_{dep}) = A_0 + \frac{(A_1 - A_0)}{\left(1 + \left(\frac{E_{dep}}{A_2}\right)^{A_3}\right)}, \quad (2.1)$$

where $A_0 = 121.916$ ps, $A_1 = 14.1263$ ps, $A_2 = 339.752$ keV, $A_3 = 2.49424$ he, the range of TOT corresponding to annihilation photons was calculated as 39642 ps - 59169 ps. The formula was determined based on the analysis described in [18].

The TOT spectrum obtained from experimental data and energy deposition spectrum obtained from the Monte Carlo simulation for all the hits in the analyzed data samples are shown in Figures 2.3a and 2.3b, respectively.

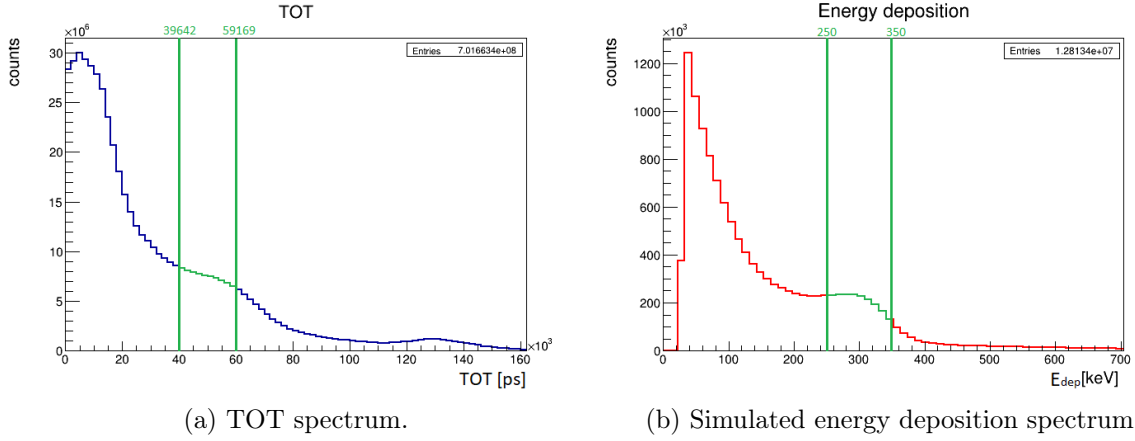


Figure 2.3: TOT and simulated energy deposition spectra with ranges corresponding to annihilation photons marked green.

In order to make sure that two photons chosen as annihilation photons were not each other's scatterings, a scatter test was performed. For two photons being candidates for annihilation ones, time difference between the measured time (time difference between two hits) and the time-of-flight (distance between hit positions \vec{x}_i, \vec{x}_j divided by the speed of light):

$$\delta_{ij} = (t_i - t_j) - \frac{|\vec{x}_i - \vec{x}_j|}{c} \quad (2.2)$$

should be less than $-0,1$ ns. Spectra of δ value obtained from the experimental data and simulation are shown in Figure 2.4.

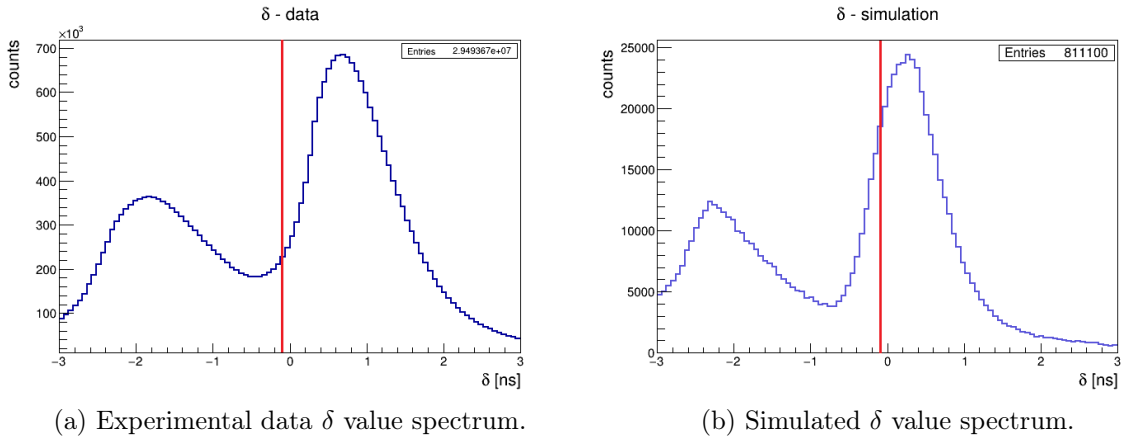


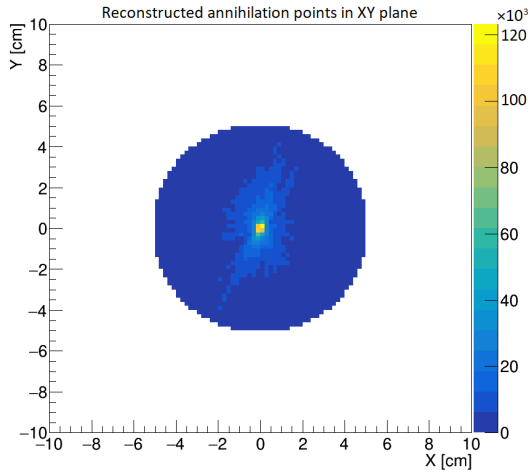
Figure 2.4: Difference between the time measured and the time-of-flight spectra with the cut marked with red line.

The cut value was chosen arbitrarily. There is a visible shift between the spectra obtained from experimental data and Monte Carlo simulation, that also appears in other analyses. Despite the fact that this problem was discussed within the group, the cause of the shift remains unknown.

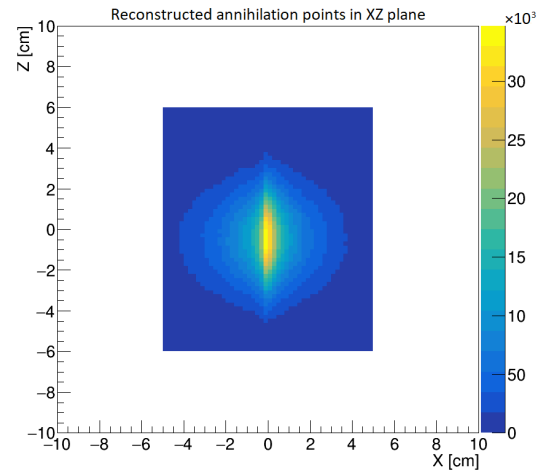
Next a cut on the angle between position vectors of the hits in XY plane (ϕ) and the measured time difference was performed. An elliptical cut was applied:

$$\left(\frac{|t_i - t_j|}{0,6 \text{ ns}}\right)^2 + \left(\frac{\phi - \pi}{0,15}\right)^2 < 1.$$

Because the annihilations were assumed to occur close to the source placed in the center of the detector, the distance of the annihilation points from the center of the detector was limited: $\sqrt{x^2 + y^2} < 5 \text{ cm}$ and $|z| < 6 \text{ cm}$. The reconstructed annihilation points images in XY and XZ plane obtained from experimental data and simulation are shown in Figures 2.5 and 2.6, respectively.

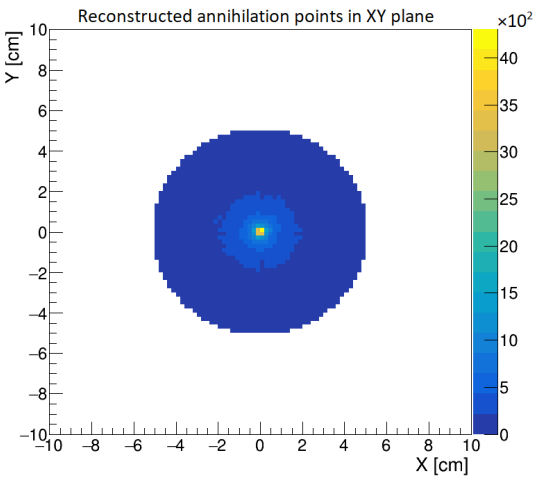


(a) Reconstructed annihilation points in XY plane.

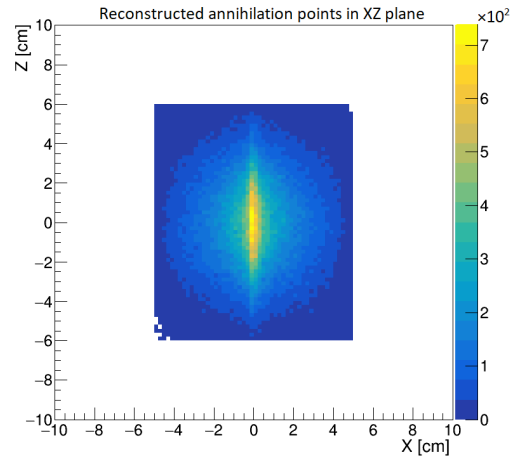


(b) Reconstructed annihilation points in XZ plane.

Figure 2.5: Reconstructed annihilation points - experimental data.



(a) Reconstructed annihilation points in XY plane.



(b) Reconstructed annihilation points in XZ plane.

Figure 2.6: Reconstructed annihilation points - Monte Carlo simulation.

A schematic diagram of scattering sequence for the Analysis 1 is shown in Figure 2.7.

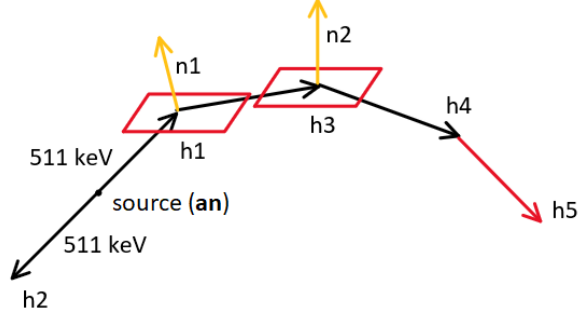


Figure 2.7: Schematic diagram of Analysis 1: scattering sequence with scattering planes marked red and unit vectors normal to them marked yellow, annihilation photons hits are denoted as h_1 , h_2 , the first and the second scatterings of one of the annihilation photons are denoted as h_3 , h_4 . A potential third scattering is marked with a red arrow and denoted as h_5 . Annihilation point is denoted as \vec{a}_n .

2.2.2. Analysis 2

For the Analysis 2 already scattered photons were chosen as the first in the sequence. Primary photons were found between two interactions in the detector. No assumptions have been made about the origin of the incident photons (h_1) causing the scatterings chosen as the first in the sequence (h_2).

A schematic diagram of scattering sequence for the Analysis 2 is shown in Figure 2.8.

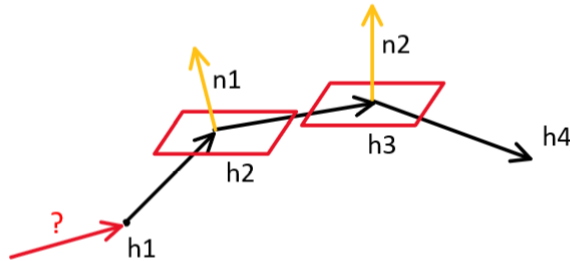


Figure 2.8: Schematic diagram of Analysis 2: scattering sequence with scattering planes marked red and unit vectors normal to them marked yellow. An unknown photon initiating first scattering is marked with a red arrow and its hit is denoted as h_1 . Hit of the first photon in the sequence is denoted as h_2 and its first and second scatterings as h_3 , h_4 .

2.2.3. Analysis 3

For Analysis 3 de-excitation photon with the energy of 1275 keV originating from the ^{22}Na source was chosen as a primary one. The choice of prompts was made based on the energy deposition (TOT).

The cut on TOT value was applied. Based on the Monte Carlo simulation, energy deposition of a photon to be considered a prompt should be greater than 400 keV. The corresponding TOT value was calculated based on the Formula 2.1: $\text{TOT} > 68063$ ps.

The TOT spectrum obtained from experimental data and energy deposition spectrum obtained from the Monte Carlo simulation for all the hits in the analyzed data samples are shown in Figures 2.9a and 2.9b, respectively.

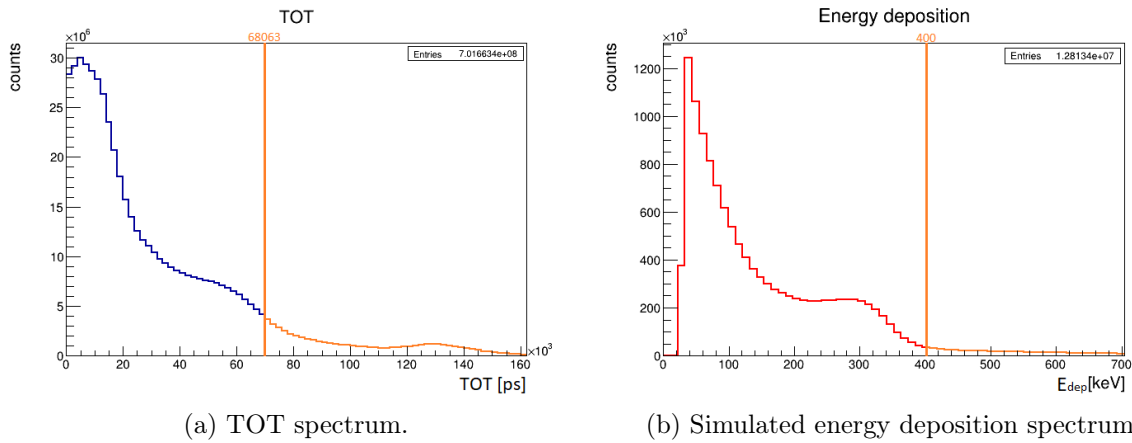


Figure 2.9: TOT and simulated energy deposition spectra with ranges corresponding to de-excitation photons marked orange.

A schematic diagram of scattering sequence for the Analysis 3 is shown in Figure 2.10.

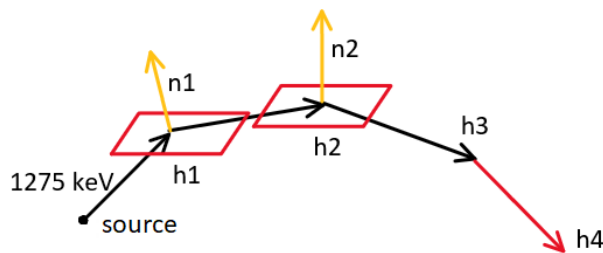


Figure 2.10: Schematic diagram of Analysis 3: scattering sequence with scattering planes marked red and unit vectors normal to them marked yellow, de-excitation photon hit is denoted as h_1 and its first and second scatterings as h_2 , h_3 . A potential third scattering is marked with a red arrow and denoted as h_4 .

Additionally, for Analysis 1 and 3, sequences starting with the first scattering of the primary photon were considered.

2.3. Angle between polarization planes

In order to find the distribution of the angle between polarization planes of incoming and scattered gamma quanta, as described in Section 2.1, a sequence of three photons being each others successive scatterings is needed.

For each of the analyses scatter selection process is the opposite of the scatter test described in Section 2.2.1. with additional conditions. The conditions were chosen to maximize sequence selection accuracy, which will be described later in this thesis. Final scatter selection process is based on five conditions:

1. In order to ensure that a pair of hits does not occur more than once in a sequence, and that the same photon is not counted as its own scattering, the indexes of previous hits in the sequence are skipped in the process.
2. The scattering (a) should be registered later than the incoming photon (n), thus time difference between scattering's (t_a) and incident gamma's (t_n) hit times should be positive. Moreover, because of detector's time resolution, if hits occur too close in time, they can get swapped. To ensure that it does not happen a cut on hit time difference is applied:

$$t_a - t_n > 0,5 \text{ ns.}$$

3. Energy deposition of the incoming photon (TOT_n) should be greater than the energy deposition of the scattering (TOT_a):

$$TOT_n > TOT_a.$$

Although the opposite may happen, it is more probable that the scattered photon deposits less energy than the incoming one. This cut is performed to optimize scatter selection accuracy.

4. Time difference between the measured time and the time-of-flight (Equation 2.2):

$$\delta_{na} > -0,1 \text{ ns.}$$

5. Finally, if more than one potential scattering is obtained for a given incoming photon, the hit for which the value of δ_{na} is closest to zero is selected as the scattering.

Knowing the positions of hits in a sequence, the directions of photons' momentum vectors are determined as:

1. Analysis 1:

$$\begin{aligned} \vec{k}_1 &= \vec{h}_1 - \vec{a}\vec{n} - \text{primary photon,} \\ \vec{k}_2 &= \vec{h}_3 - \vec{h}_1 - \text{first scattering,} \\ \vec{k}_3 &= \vec{h}_4 - \vec{h}_3 - \text{second scattering,} \end{aligned}$$

where $\vec{h}_1, \vec{h}_3, \vec{h}_4, \vec{a}\vec{n}$ are described in the caption of Figure 2.7.

2. Analysis 2:

$$\begin{aligned}\vec{k}_1 &= \vec{h}_2 - \vec{h}_1 - \text{primary photon,} \\ \vec{k}_2 &= \vec{h}_3 - \vec{h}_2 - \text{first scattering,} \\ \vec{k}_3 &= \vec{h}_4 - \vec{h}_3 - \text{second scattering,}\end{aligned}$$

where $\vec{h}_1, \vec{h}_2, \vec{h}_3, \vec{h}_4$ are described in the caption of Figure 2.8.

3. Analysis 3:

$$\begin{aligned}\vec{k}_1 &= \vec{h}_1 - \text{primary photon,} \\ \vec{k}_2 &= \vec{h}_2 - \vec{h}_1 - \text{first scattering,} \\ \vec{k}_3 &= \vec{h}_3 - \vec{h}_2 - \text{second scattering,}\end{aligned}$$

where $\vec{h}_1, \vec{h}_2, \vec{h}_3$ are described in the caption of Figure 2.10.

Angle between polarization planes (α) is determined as the angle between normal versors to the scattering planes (\hat{n}_1, \hat{n}_2):

$$\alpha = \arccos \hat{n}_1 \cdot \hat{n}_2,$$

where $\hat{n}_1 \cdot \hat{n}_2$ - scalar product of the vectors.

Chapter 3

Sequence selection accuracy

3.1. Monte Carlo simulation

The Monte Carlo simulation was performed using J-PET-Geant4 software, which is a Monte Carlo simulation program designed for the J-PET detector created in Geant4 toolkit. The simulation generates information about gamma quanta interactions that are further processed in the same manner as experimental data. In Geant4 physics package LivermorePolarized-Physics is used. This package generates a full simulation of all physical processes occurring in the experiment, including electron-positron annihilations and polarized Compton scatterings.

3.2. Determination of sequence selection accuracy

The sequence selection accuracy for each of the analyses was estimated based on the Monte Carlo simulation. For the sequence to be considered correctly identified, hits identified in the sequence had to meet the following conditions:

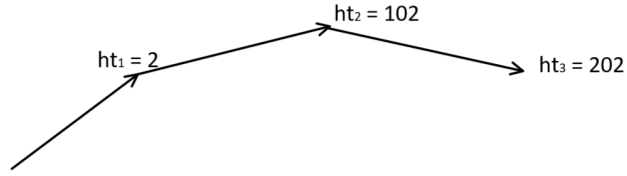
1. All hits identified in the sequence must originate from the same event (this is possible in the Monte Carlo simulation due to the flag which marks the vertex of a given event).
2. All of the hits identified in the sequence should have proper hit types corresponding to their origin. In the simulation hit type of prompts is denoted as 1 and of annihilation photons as 2, every scattering adds 100 to the hit type (Figure 3.1).
3. To check if a photon found between two interactions in the detector actually made the way between those hit positions, the angle between simulated photon momentum vector and a vector connecting simulated hit positions (φ) is checked (Figure 3.2). For a photon to be considered correctly reconstructed $\varphi < 0,01$ rad.

Based on the Monte Carlo simulation, sequence selection accuracy was estimated for all of performed analyses. Sequence selection accuracy is calculated as a percentage of correctly identified sequences (N_c) out of all identified ones (N):

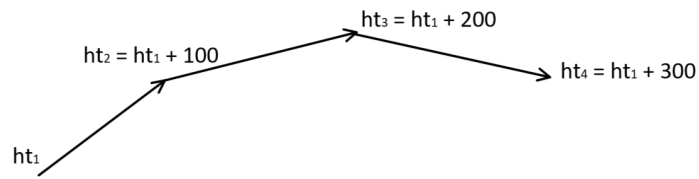
$$A = \frac{N_c}{N} \cdot 100\%.$$

Sequence selection accuracy estimated for Analysis 1, 2 and 3 is shown in Table 3.1.

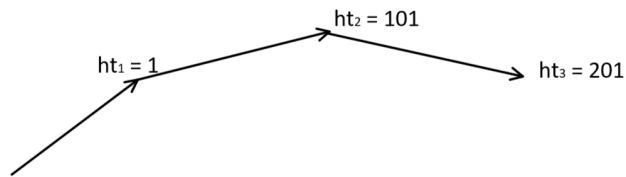
For sequences starting with the first scattering of a primary photon in Analysis 1, not enough data was analyzed to estimate sequence selection accuracy.



(a) Analysis 1.



(b) Analysis 2.



(c) Analysis 3.

Figure 3.1: Schematic diagrams of scattering sequences for Analysis 1, 2 and 3 with hit types marked.

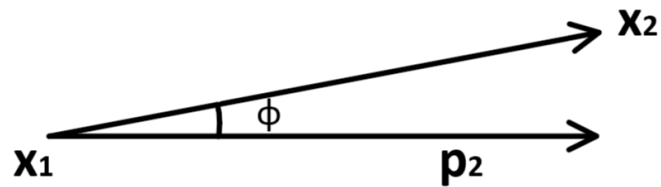


Figure 3.2: Schematic diagram of photon momentum vector (\vec{p}) and vector connecting simulated hit positions (\vec{x}_1, \vec{x}_2) with the angle between them (φ) marked.

Table 3.1: Sequence selection accuracy estimated for Analysis 1, 2 and 3 with numbers of correctly and all identified sequences.

Type of analysis	All identified sequences	Correctly identified sequences	Selection accuracy
1	1580	897	56.77%
1 sequences starting with the first scattering of the annihilation photon	3	2	-
2	856	308	35.98%
3	78248	24659	31.51%
3 sequences starting with the first scattering of the prompt photon	378	98	25,93%

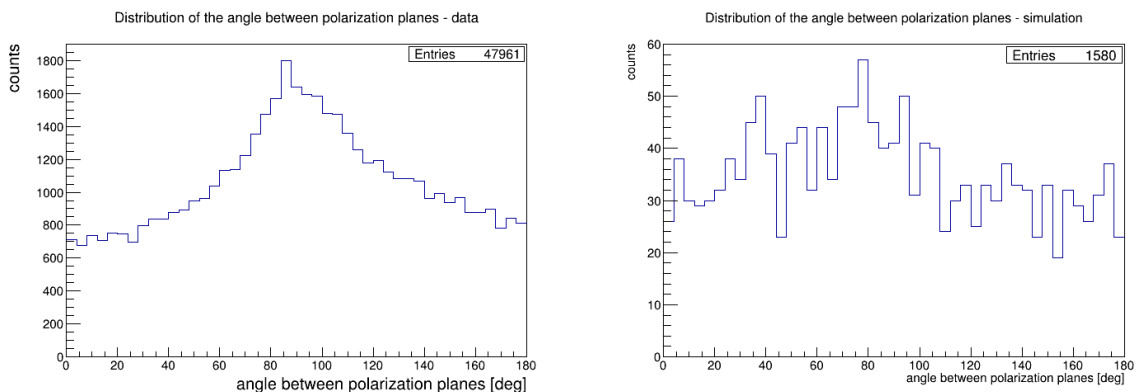
Chapter 4

Results

The results of this study are histograms showing the distribution of the angle between polarization planes obtained from experimental data as well as from the Monte Carlo simulation. Comparisons of those results obtained from every type of analysis are shown in Figures 4.1 - 4.5.

4.1. Analysis 1

Distributions obtained from experimental data, from the sequences starting with the annihilation photons show a peak structure forming around $80^\circ - 90^\circ$ (Figure 4.1a). Histograms obtained from Monte Carlo simulations show a similar, yet less defined peak structure (Figure 4.1b).

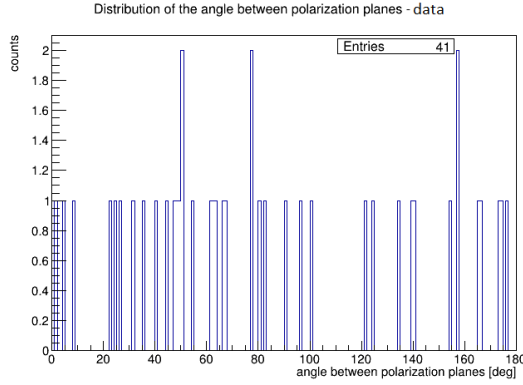


(a) Results obtained from experimental data.

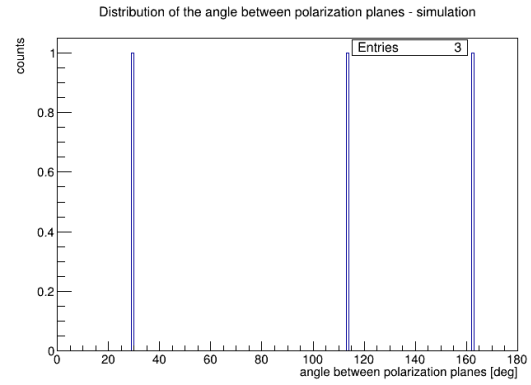
(b) Results obtained from Monte Carlo simulation.

Figure 4.1: Distribution of the angle between polarization planes of annihilation gamma quantum and its scattering.

For Analysis 1, sequences starting with the first scattering of the annihilation photon were also considered. However not enough data was analyzed and obtained distributions cannot undergo further interpretation (Figure 4.2).



(a) Results obtained from experimental data.

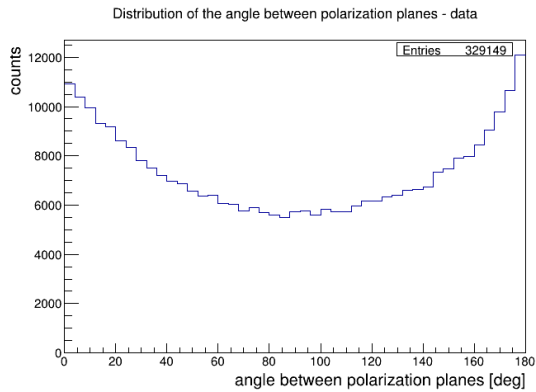


(b) Results obtained from Monte Carlo simulation.

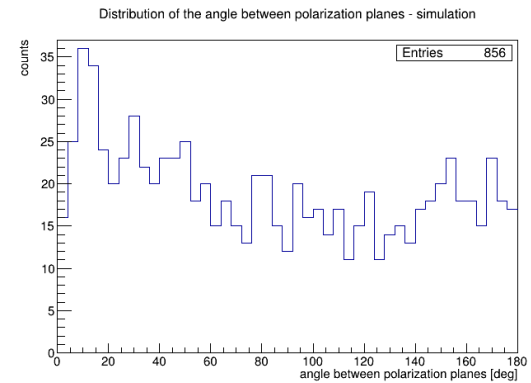
Figure 4.2: Distribution of the angle between polarization planes of the first and the second scattering of the annihilation photon.

4.2. Analysis 2

Distributions obtained from the sequences starting with a photon found between two interactions in the detector (an already scattered gamma quantum with unknown origin) show enhancements around 0° and 180° (Figure 4.3a). Again, the results are similar for experimental data and Monte Carlo simulation, with less defined structures visible in the histogram obtained from the latter (Figure 4.3b).



(a) Results obtained from experimental data.



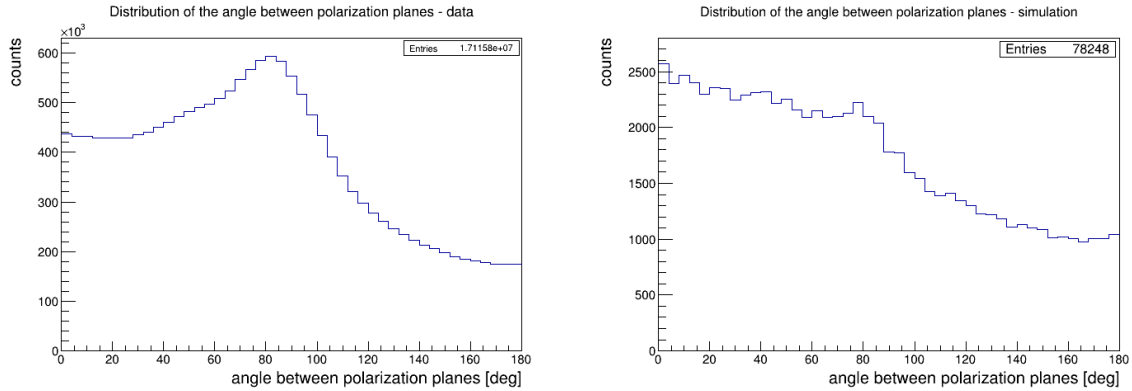
(b) Results obtained from Monte Carlo simulation.

Figure 4.3: Distribution of the angle between polarization planes of incoming and scatter gamma quanta, where incident photon was found between two interactions in the detector.

4.3. Analysis 3

Similarly to the distributions obtained from the Analysis 1 (Figure 4.1), a peak structure forming around $80^\circ - 90^\circ$ is shown in the histograms obtained from experimental data (Figure 4.4a) and Monte Carlo simulation (Figure 4.4b). As for the Analysis 1, the peak structure

visible in the histogram obtained from the simulation is less enhanced.

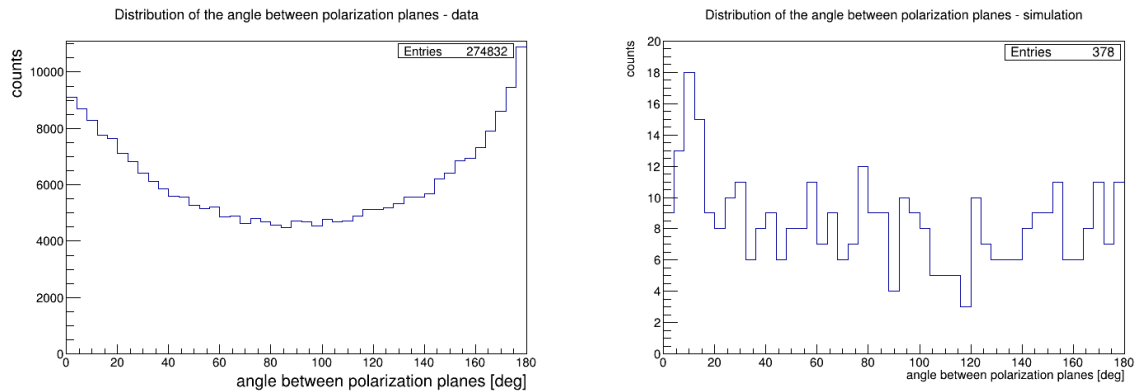


(a) Results obtained from experimental data.

(b) Results obtained from Monte Carlo simulation.

Figure 4.4: Distribution of the angle between polarization planes of de-excitation gamma quantum and its scattering.

As for the Analysis 1, sequences starting with the first scattering of the primary photon were considered. However, for Analysis 3, enough sequences were obtained from the experimental data for further analysis. Obtained distributions are similar to the results of Analysis 2. Histogram shows enhancements around 0° and 180° (Figure 4.5a). However, due to small statistics in the result obtained from the Monte Carlo simulation the distribution is not clearly visible (Figure 4.5b).



(a) Results obtained from experimental data.

(b) Results obtained from Monte Carlo simulation.

Figure 4.5: Distribution of the angle between polarization planes of the first and the second scattering of the de-excitation photon.

Chapter 5

Conclusions

Comparing the results of each analysis performed in frame of this work, the distributions obtained from the sequences starting with annihilation (Analysis 1) and de-excitation photons (Analysis 3) are very similar. Both histograms show a peak structure forming around 80° - 90° . Different distribution shape - an enhancement around 0° and 180° is visible in the case of the sequences starting with a photon found between two interactions in the detector (Analysis 2) and the first scattering of the de-excitation photon. However, the origin of the incident photon causing the scattering chosen as primary for Analysis 2 was not assumed. Hence, all of the sequences starting with the first scattering of the de-excitation photon were also included in the Analysis 2 and had a significant impact on the shape of the distribution. About 83,5% of the results obtained from the experimental data and about 44,2% of the results obtained from the simulation came from the sequences starting with the first scattering of the prompt photon. Differences in the shape of obtained distributions may result from different origins of the primary photons for each pair of the analyses. For Analysis 1 and 3, first photon in the scattering sequence originated from the source, whereas for Analysis 2 and sequences starting with the first scattering of the prompt, primary photon has already undergone Compton scattering in the detector. However, the difference may also be the result of the J-PET detector geometry and its limitations.

Despite the fact that there is some similarity between the results obtained from experimental data and Monte Carlo simulations, for now it is not possible to unambiguously determine whether the shapes of the distributions were the result of physical phenomena or whether they resulted from the geometry of the detector.

In order to find the distribution of the angle between polarization planes of the incoming and scattered gamma quanta, it is necessary to eliminate the influence of the detector geometry on the distribution as precisely as possible. The next step of this study should be the analysis of the simulation generated in such a way that it does not include the polarization part of the Klein-Nishina formula and extrapolate the results to the distributions obtained from the experimental data.

Chapter 6

Summary

The aim of this thesis was to investigate the polarization of high-energy photons in Compton scattering, precisely to find the distribution of the angle between polarization planes of the incoming and scattered gamma quanta. In order to do so, three types of analysis were performed based on the analysis of the momentum directions of the incoming photon and two subsequent scatterings. The types of analysis differed in the origin and energy of the incident gamma quantum: (i) electron-positron annihilation photon with the energy of 511 keV, (ii) already scattered photon found between two interactions in the detector with an unknown energy, (iii) ^{22}Ne de-excitation photon with the energy of 1275 keV. Analysis was performed on the experimental data as well as on Monte Carlo simulation. The experimental data was collected during J-PET Run 11 using ^{22}Na source placed in the center of the detector and the Monte Carlo simulation was generated using J-PET-Geant4 software. Although obtained results seem promising, it is necessary to eliminate the influence of the J-PET detector geometry on the angular distributions and analyze the simulation generated excluding the polarization part of the Klein-Nishina formula.

Bibliography

- [1] Aspect, A., Dalibard, J. & Roger, G. Experimental test of Bell's inequalities using time-varying analyzers. *Phys. Rev. Lett.* 49, 1804-1809 (1982).
- [2] Weihs, G. et al. Violation of Bell's inequality under strict Einstein locality conditions. *Phys. Rev. Lett.* 81, 5039-5043 (1998).
- [3] Hecht, E. *Optyka*. Red. Makowski, M. Warszawa: Wydawnictwo Naukowe PWN, (2012), p. 329-330.
- [4] Klein, O. & Nishina, Y. Über die Streuung von Strahlung durch freie Elektronen nach der neuen relativistischen Quantendynamik von Dirac. *Zeitschrift für Physik* 52, 853–868 (1929).
- [5] Moskal, P. et al. Feasibility studies of the polarization of photons beyond the optical wavelength regime with the J-PET detector. *Eur Phys. J. C* 78, 970 (2018).
- [6] Hiesmayr, B.C. & Moskal, P. Genuine Multipartite Entanglement in the 3-Photon Decay of Positronium. *Sci. Rep.* 7 15349 (2017).
- [7] Moskal, P. Strip device and method for determining the location and time of reaction of the gamma quanta and the use of the device to determine the location and time of reaction of the gamma quanta in positron emission tomography. US Patent App. 13/383,582. (2012).
- [8] Moskal, P. Strip device and method for determining the location and time of reaction of the gamma quanta and the use of the device to determine the location and time of reaction of the gamma quanta in positron emission tomography. EP Patent 2,454,612. (2015).
- [9] Slomka, P. J., Pan, T. & Germano, G. Recent Advances and Future Progress in PET Instrumentation. *Seminars in Nuclear Medicine* 46, 5–19 (2016).
- [10] Moskal, P. et al. Feasibility study of the positronium imaging with the J-PET tomograph. *Phys. Med. Biol.* 64 (2019).
- [11] Moskal, P. & Stepień, E. Ł. Prospects and clinical perspectives of total-body PET imaging using plastic scintillators. *PET Clin.* 15, 439-452 (2020).
- [12] Moskal, P. et al. Positronium imaging with the novel multiphoton PET scanner. EABH4394 *Science Advances* 7 (2021).
- [13] Moskal, P. et al. Testing CPT symmetry in ortho-positronium decays with positronium annihilation tomography. *Nature Communications* 12, 5658 (2021).

- [14] Moskal, P. et al. Potential of the J-PET detector for studies of discrete symmetries in decays of positronium atom - a purely leptonic system. *Acta Phys. Polon.* B47, 509 (2016).
- [15] Moskal, P. et al. STRIP-PET: a novel detector concept for the TOF-PET scanner. *Nucl. Med. Rev.* 15C, 68–69 (2012).
- [16] Moskal, P. et al. TOF-PET detector concept based on organic scintillators. *Nucl. Med. Rev.* 15C, 81–84 (2012).
- [17] Niedźwiecki, S. et al. J-PET: A New Technology for the Whole-body PET Imaging. *Acta Phys. Polon.* B48, 1567-1576 (2017).
- [18] Sharma, S. et al. Estimating relationship between the Time Over Threshold and energy loss by photons in plastic scintillators used in the J-PET scanner. *EJNMMI Phys.* 7, 39 (2020).
- [19] Kacprzak, K. J-PET Data Analysis with Framework software version 10.0. (2022). Unpublished internal report.
- [20] Chug, N. J-PET Run 11. (2020). Unpublished internal report.
- [21] Chhokar, J. & Niedźwiecki, S. J-PET Run 9. PET UJ Raport nr 9/2019 (2019). Unpublished internal report.
- [22] Dryzek, J. Wstęp do spektroskopii anihilacji pozytonów w ciele stałym. Wydawnictwo UJ, Cracow (1997), p. 11 - 18.
- [23] Jasińska, B. & Moskal, P. A New PET Diagnostic Indicator Based on the Ratio of $3\gamma/2\gamma$ Positron Annihilation. *Acta Phys. Polon.* B48, 1577-1577 (2017).